



TECHNICAL ARTICLE

# Effect of B<sub>4</sub>C Addition on Microstructure and Wear Resistance of Laser Cladding NiCrBSi Coatings

HONGLIANG MA,<sup>1</sup> YUNLONG LIANG,<sup>1</sup> and HANGUANG FU <sup>1,2</sup>

1.—Key Laboratory of Advanced Functional Materials, Ministry of Education, School of Materials Science and Engineering, Beijing University of Technology, Number 100, Pingle Garden, Chaoyang District, Beijing 100124, People's Republic of China. 2.—e-mail: hgfu@bjut.edu.cn

In order to solve the problems of low hardness and poor wear resistance of titanium alloy, laser cladding technology was used to prepare NiCrBSi coatings with different amounts of B<sub>4</sub>C on the surface of Ti-6Al-4V alloy. The effects of B<sub>4</sub>C content on the microstructure evolution, hardness, fracture toughness, and wear resistance of NiCrBSi coatings were investigated. The results showed that with an increase of B<sub>4</sub>C addition, the size and number of ceramic phases TiB<sub>2</sub>, TiC, and CrB in the coating increased, and the ceramic phases were dispersed in the coating. The average microhardness of the coating with 9 wt.% B<sub>4</sub>C addition was the highest, reaching 1250.3 HV<sub>0.2</sub>, which is 15% higher than that of the coating without B<sub>4</sub>C addition. After adding B<sub>4</sub>C, the fracture toughness of the coating increased. When the addition of B<sub>4</sub>C was 3 wt.%, the fracture toughness of the coating was the highest, reaching 1.42 MPa m<sup>1/2</sup>, which is 178.4% higher than that of the coating without B<sub>4</sub>C. With the increase of the addition of B<sub>4</sub>C, the wear loss of the coating decreased and the wear resistance increased.

## INTRODUCTION

Titanium alloy has many advantages, such as high specific strength and good corrosion resistance, so it is widely used in aerospace, biomedical, and military fields. In practical use, titanium alloy has some problems such as low hardness and poor wear resistance, which limits its application in friction and wear environments.<sup>1</sup> Titanium has strong adhesion and a high friction coefficient, and it is easy to produce serious adhesive wear in use. This is related to its electronic configuration, crystal structure, and lubrication properties.<sup>2</sup> In order to solve the above problems, many researchers have changed the surface properties of titanium alloy by using thermal spraying technology,<sup>3</sup> gas phase deposition,<sup>4</sup> ion implantation,<sup>5</sup> laser remelting,<sup>6</sup> laser cladding,<sup>7</sup> and so on. Among them, laser cladding uses laser irradiation to melt and rapidly solidify materials with special properties and substrates to form metallurgical bonds. Laser cladding has been

widely used in industrial production because of its high uniformity, high deposition rate and low matrix dilution.

The composite coating obtained by laser cladding metal and ceramic particle reinforced phase on the surface of titanium alloy has always been a research hotspot. The metal or alloy in the composite coating has good strength and toughness, and functions as a region of transition and buffer. As the bonding phase between the ceramic reinforcing phase and the substrate, it effectively reduces the residual stress and cracking tendency of the coating. The ceramic phase plays the role of wear resistance and high temperature resistance. In addition, the ceramic particles may participate in chemical reactions in the process of laser cladding to form new phases with required properties. Yang et al.<sup>8</sup> prepared three kinds of pure coatings, Co, Co-Ti<sub>3</sub>SiC<sub>2</sub>, and Co-cu/Ti<sub>3</sub>SiC<sub>2</sub>, on the surface of Ti-6Al-4V by laser cladding. The coatings produced high microhardness (CoTi<sub>2</sub>/TiC) and good toughness (CoTi), and the microhardness increased to 2.1–2.5 times that of the substrate (370 HV<sub>0.5</sub>). Zhou et al.<sup>9</sup> prepared Ni60-TiC-WS<sub>2</sub> mixed powder composite coating on Ti6Al4V alloy by laser cladding. The experimental

(Received July 4, 2022; accepted November 13, 2022;  
published online December 5, 2022)

**Table I. Chemical composition of Ti-6Al-4V and NiCrBSi (Ni45) powders (wt.%)**

Materials	Al	V	Fe	C	N	H	O	Ti
Ti-6Al-4V	6.1–5.9	4.2–3.9	0.30	0.10	0.05	0.015	0.20	Bal
Ni45	3.05 Si	1.89 B	5.28	0.33	10.01 Cr	Ni: Bal		

results showed that the microhardness of the composite coating was higher than that of the substrate, and the wear resistance and antifriction properties of the composite coating were better than those of the substrate at 20°C, 300°C, 600°C, and 800°C, due to the synergistic effect of in-situ synthesized solid lubricant and hard phase.

Nickel-based alloy is an alloy with excellent all-round properties: high strength, excellent oxidation resistance, and corrosion resistance. Li et al.<sup>10</sup> studied the strengthening mechanism of spherical WC and non-spherical WC reinforced Inconel 625 composite coatings by laser melt deposition. Partial decomposition of WC occurs in the process of laser deposition, in which the decomposition of non-spherical WC was more serious, and the C and W elements in WC were diffused into the IN625 matrix. The decomposition of WC and other elements in the coating formed new phases such as WC, W<sub>2</sub>C, NbC, W<sub>6</sub>C<sub>2.54</sub>, M<sub>23</sub>C<sub>6</sub>, and so on. The microhardness, wear resistance and corrosion resistance of the matrix were improved. Xia et al.<sup>11</sup> used circular oscillating laser deposition of GH3536 nickel base superalloy, GH3536-16 wt.% coarse WC, and GH3536-16 wt.% fine WC composites. Compared with GH3536, the average microhardness of the composite increased by 59.70% (coarse WC) and 74.66% (fine WC), and the wear rate decreased by 84.87% (coarse WC) and 89.17% (fine WC), respectively.

TiB<sub>2</sub> is a very hard (25–35 GPa) ceramic with a high melting point (3225°C) and low density (4.52 g/cm<sup>3</sup>).<sup>12</sup> These excellent properties make TiB<sub>2</sub> a cutting-edge strengthening material to improve the mechanical properties of metal matrix. TiC has strong combining power and good stability, so it is easy to grow in situ. Also, the Vickers hardness of TiC is higher than 3000 HV and the melting point is 3160°C, which is beneficial in improving the wear resistance of the coating.<sup>13</sup> Therefore, TiC is often used as a coating reinforcement. Bai et al.<sup>14</sup> prepared the composite coatings containing TiC and Ti<sub>2</sub>Ni matrix on Ti-6Al-4V by laser cladding. The composite coating consisted of Ni-based alloy and different contents of B<sub>4</sub>C (0 wt.%, 5 wt.%, 15 wt.%, and 25 wt.%). The coating was mainly composed of matrix TiNi/Ti<sub>2</sub>Ni and reinforcing particles TiC/TiB<sub>2</sub>. The average microhardness of the coating increased with the increase of B<sub>4</sub>C content. The addition of B<sub>4</sub>C (5 wt.% and 15 wt.%) reduced the wear volume of the coating. Diao et al.<sup>15</sup> prepared TiC/TiB<sub>2</sub> composite coating on the surface of TC2

titanium alloy by Ti/TiC/TiB<sub>2</sub> powder laser cladding technology. The cladding layer was composed of Ti, TiC, and TiB<sub>2</sub>. After laser cladding, the maximum hardness of the laser cladding surface layer reached 1100 HV, which is more than 3 times higher than that of the TC2 substrate (300 HV).

Because of its strong Cr-B and zigzag B-B bonding network, CrB has excellent mechanical properties and Vickers hardness up to 2100–2200 HV.<sup>16</sup> Compared with carbide ceramics, boride ceramics have stronger oxidation resistance at high temperature and can work at 1400°C. In some studies,<sup>17,18</sup> a high hardness laser cladding layer was obtained on the surface of titanium alloy by presetting nickel-based powder and B<sub>4</sub>C powder, but the influence of different composition powders on its mechanical properties and composition phase was not explored. In order to further improve the wear resistance of NiCrBSi coating on titanium alloy, on the basis of previous research,<sup>19</sup> B<sub>4</sub>C powder was added to NiCrBSi alloy powder which contained 30 wt.% Cr<sub>3</sub>C<sub>2</sub> to form TiB<sub>2</sub>, TiC, and CrB reinforcement phase by in-situ reaction. The effect of different amounts of B<sub>4</sub>C on the microstructure and properties of laser cladding NiCrBSi composite coating on titanium alloy surface was investigated, and an obvious improvement in wear resistance of laser cladding B<sub>4</sub>C composite coating on titanium alloy surface was expected.

## EXPERIMENTAL

### Materials and Laser Cladding Process

The base metal was annealed Ti-6Al-4V, and its chemical composition is shown in Table I. An angle grinder was used to smooth the surface, then it was polished with 240 grit sandpaper and scrubbed with alcohol and acetone. The coating material was NiCrBSi alloy powder, its chemical composition is shown in Table I, and the particle size range of the powder was 75–105 μm. The metal powder was expelled by coaxial powder feeding under the action of argon flow. The amount of powder was adjusted to 15 g/min. The purity of the Cr<sub>3</sub>C<sub>2</sub> and B<sub>4</sub>C powders was 99.99%, and the particle size range was 75–105 μm. B<sub>4</sub>C was added to the NiCrBSi powder with 30 wt.% Cr<sub>3</sub>C<sub>2</sub> added (0 wt.%, 3 wt.%, 6 wt.%, 9 wt.%), respectively. The powder with the required ratio was mixed in a ball mill for 1.5 h, then dried in a drying box at 60°C for 2 h.

The laser cladding equipment used was an IPG fiber laser (model: YLS-6000-S2), laser wavelength

1070 nm. A square spot with size 5 mm × 5 mm was output through the laser lens, and the laser power was 2000 W. ABB's six-axis linkage robot was used to control the cladding head to carry out the cladding tests according to a set program, and the scanning speed was 5 mm/s. During the experiment, high purity argon was used to protect the molten pool from oxidation. The gas flow was set to 15 l/min. The sample number and composition (mass fraction, %) of the composite coatings were designated as follows: B0 (Ni45 + 30 Cr<sub>3</sub>C<sub>2</sub> + 0 B<sub>4</sub>C), B1 (Ni45 + 30 Cr<sub>3</sub>C<sub>2</sub> + 3 B<sub>4</sub>C), B2 (Ni45 + 30 Cr<sub>3</sub>C<sub>2</sub> + 6 B<sub>4</sub>C), and B3 (Ni45 + 30 Cr<sub>3</sub>C<sub>2</sub> + 9 B<sub>4</sub>C).

### Microstructure Analysis

The samples were mechanically polished to 2000 grit and polished with a polishing cloth. Then the samples were etched in a mixed solution of HF, HNO<sub>3</sub>, and H<sub>2</sub>O at 1:3:7 for about 15 s. An optical microscope (OM, OLYMPUS BX51M) and field emission scanning electron microscope (SEM, SUPRA55) were used to observe the macroscopic morphology and microstructure of the coating, and an energy dispersive spectrometer (Oxford) was used to determine the element distribution and phase composition. After ion thinning, the samples were observed by transmission electron microscope (TEM, JEM-2100F); bright field images and diffraction spots were obtained, and the phase was determined. Using a Bruker D8 diffractometer, the phase structure at 40 kV and 40 mA was analyzed by XRD using copper K $\alpha$  radiation (radiation wavelength 1.54056 nm) as the x-ray source. In the range of 2 $\theta$  (20–80°), the step-scanning mode (0.02°/step) was used to scan the sample.

### Mechanical Properties and Wear Test

The microhardness was tested by a digital microhardness tester (MICROMET-5103, load 200 g, residence time 10 s). In the direction of the cross section of the cladding layer, the microhardness was measured at different distances from the upper surface of the coating, and three points were measured and averaged at the same depth. Fracture toughness refers to the ability of materials to resist unstable crack propagation under certain loads. The fracture toughness of the coatings was measured by the Vickers indentation method to evaluate cracking sensitivity. First of all, Vickers indentation was done on the cross section of the coating under a load of 5 kg for 15 s using an HVS-30ZC Vickers microhardness tester. Then, the indentation and cracks around the indentation were observed and measured under the optical microscope (OM) to obtain the size of the indentation and the length of the crack. A schematic diagram of an indentation with cracks is shown in Fig. 1.

Fracture toughness was calculated by using the Evans Wilshaw model.<sup>20</sup> Laser cladding coating containing a large number of ceramic reinforced

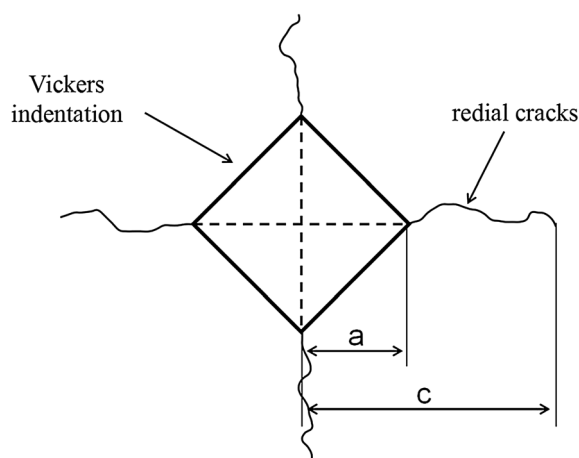


Fig. 1. Schematic of crack formation by Vickers indentation.

materials is hard and brittle, and the fracture toughness of cladding coating<sup>6,21,22</sup> has been measured in many studies. The fracture toughness of the coating is derived from the following formula:

$$K_{IC} = 0.079 \left( P/a^{3/2} \right) \log(4.5a/c) \quad (1)$$

where  $K_{IC}$  is the fracture toughness (MPa m<sup>1/2</sup>),  $P$  is the applied load (N),  $a$  is half the diagonal length (m) of the indentation,  $c$  is half the diagonal length plus half the crack length (m). The value of  $a$  should be between 0.6 and 4.5.

The wear test for the coating was carried out by using a high-speed ring block friction and wear tester (MRH-3w). The specific parameters were: rotational speed 200 r/min, ring block made from GCr15 steel, ring block hardness 60 HRC, test load 196 N, wear time 2 h. The weight of the sample was found using an analytical balance with an accuracy of 0.1 mg, and the wear data were the average of three tests. The reciprocal of weight loss is used to characterize the wear resistance of the coating. After the wear experiment, the morphology of the worn surface was observed and analyzed by scanning electron microscope (SEM) and laser confocal microscope (OLS40-CB).

## RESULTS AND DISCUSSION

### Microstructure and Phase Analysis

The surface of the cladding coating with different amounts of B<sub>4</sub>C was polished and analyzed by XRD. The diffraction peaks were calibrated according to the results of the JCPDS card index of the Joint Committee of Diffraction Standards. The coatings were mainly composed of  $\gamma$ -Ni, Ni<sub>3</sub>Ti, NiTi, TiB<sub>2</sub>, TiC, CrB, and so on, as shown in Fig. 2. In the process of laser cladding, the added Cr<sub>3</sub>C<sub>2</sub> and B<sub>4</sub>C undergo decomposition reactions (2) and (3) to produce Cr, C, and B elements. Due to the dilution effect of laser cladding, the Ti elements in the

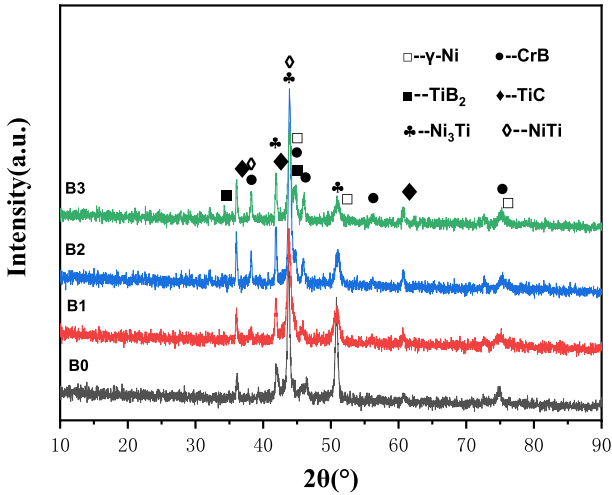
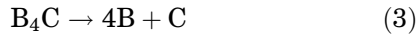


Fig. 2. X-ray diffraction of cladding layers with different  $B_4C$  content.

matrix were fully mixed with the cladding powder under the action of Marangoni convection.<sup>23</sup> Reactions (3), (4), and (5) occurred.



It was calculated in reference<sup>24</sup> that the Gibbs free energy change of the above reaction Eqs. 2–6, within a certain temperature range, was negative and could occur spontaneously. It was also found that the addition of  $B_4C$  could enhance the intensity of the CrB phase diffraction peak. In addition, the intensities of the diffraction peaks of  $TiB_2$  and TiC phases were also slightly enhanced.

The microstructure of the coating with  $B_4C$  addition was observed under a scanning electron microscope. There were mainly medium-gray and black bulk particles in the coating, and they showed compound growth. In addition, there were long strips of a light-gray hue. The size and number of black bulk particles increased with the increase of the mass fraction of  $B_4C$ . At the same time, the number of medium-gray particles grew, and were dispersed in the coating. In addition, the light-gray strips also grew in numbers after the addition of  $B_4C$ , as shown in Fig. 3b–d. The content of ceramic reinforcement phase in Fig. 3 was calculated by ImageJ software, as shown in Table II. With the increase of  $B_4C$  content, the  $TiB_2$  content increased from 1.5 vol.% to 11.9 vol.%, the TiC content

increased from 10.3 vol.% to 20.7 vol.%, and the CrB content increased from 6.4 vol.% to 18.7 vol.%.

The precipitates in the cross section of the B2 coating were analyzed by EDS surface scanning and point scanning. The microstructure was mainly composed of cellular dendritic precipitated phase (A), black massive precipitated phase (B), strip precipitated phase (C), light gray matrix (D) and dark gray matrix (E), as shown in Fig. 4 and Table III. The cellular dendritic phase (A) was mainly composed of Ti, C and B elements, as shown in Fig. 4a. Similar phases have been found in many studies.<sup>14,25</sup> Combined with the results of the spot scan and XRD in Table III, it was inferred that the cellular dendritic phase (A) was TiC, and some boron elements existed in TiC in the form of solid solution. The primary crystal of TiC is a regular octahedral crystal composed of Ti and C atoms, and a pyramid is formed because of its different growth rate in the  $\langle 100 \rangle$  direction. New bulges are produced under the action of the tip temperature gradient, and continue to split and grow to form dendrites.<sup>26</sup> The massive precipitated phase (B) mainly contains Ti element and B element, and it is generally quadrilateral and hexagonal, and it was inferred that it had a three-dimensional hexagonal prism structure.  $TiB_2$  has a close-packed hexagonal structure. Combined with the results of XRD, it was inferred that the black bulk precipitate was  $TiB_2$ . Further observation showed that most of the cellular dendritic phase TiC and black massive particles  $TiB_2$  grew with each other. Because the Gibbs free energy of the reaction to form  $TiB_2$  is lower than that of TiC, the bulk  $TiB_2$  precipitates preferentially. At the same time, Ti and C elements were enriched around it, and when the condition of TiC nucleation was reached,  $TiB_2$  nucleation began and increased by way of non-uniform nucleation. The precipitate strips (C) are mainly rich in Cr and B elements. It can be seen in Table III that the atomic ratio of Cr element to B element is about 1:1. Combined with the results of XRD scanning, the strip precipitates (C) were judged to be CrB. The light gray matrix (D) was also mainly composed of Ti and Ni elements. The atomic ratio of Ti to Ni was 1:3, which was inferred to be  $Ni_3Ti$ . The gray petal phase (E) was mainly rich in Ni elements, and some elements such as Al and Fe were dissolved in the form of solid solution. Combined with XRD, it was inferred that it was  $\gamma$ -Ni.

The bright field phase and selected area diffraction picture of the cladding layer of the B3 sample under the transmission electron microscope are shown in Fig. 5. The long strip phase can be observed in Fig. 5a, combined with the morphology observed by SEM. It was found that it was similar to the long strip rich in Cr and B elements under the scanning electron microscope. Figure 5c shows the selected area diffraction picture of the long strip phase. The results showed that the interplanar spacing of (200), (221) and (021) is 1.52, 1.29 and

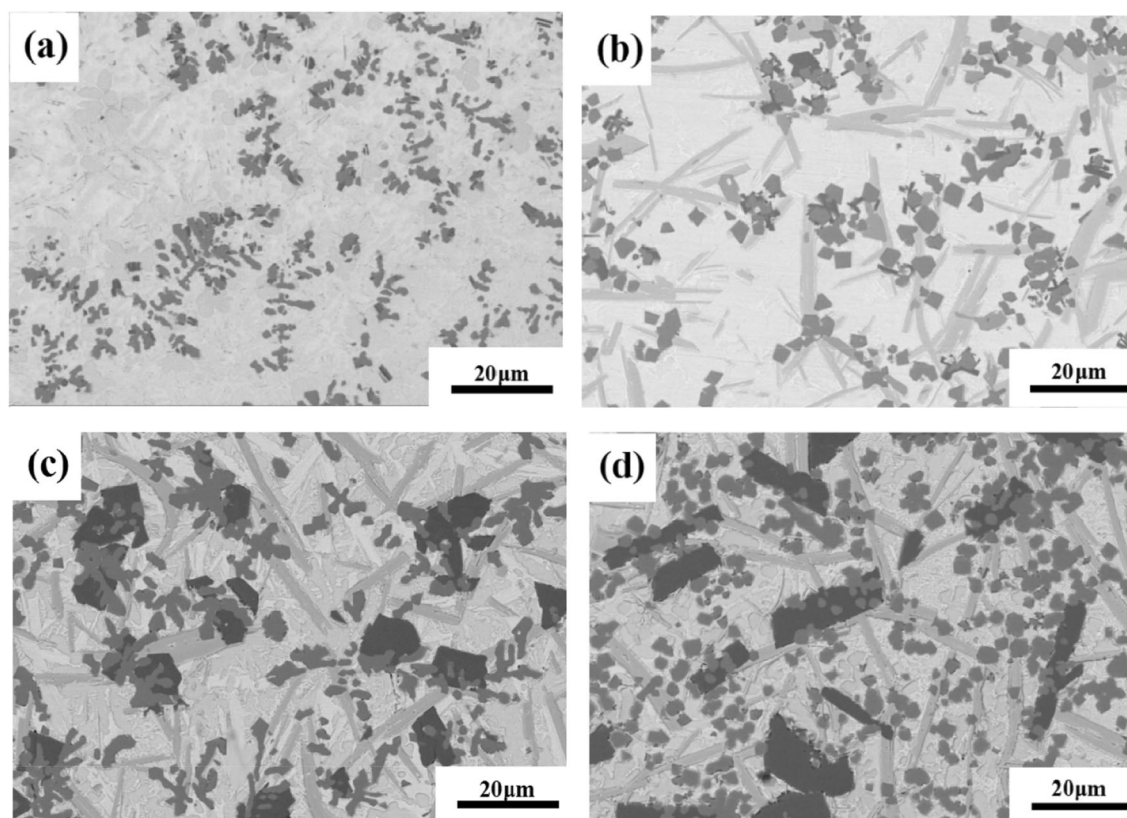


Fig. 3. SEM images of cross sections of different B<sub>4</sub>C content coatings: (a) 0 wt.%; (b) 3 wt.%; (c) 6 wt.%; (d) 9 wt.%.

**Table II. Content of ceramic reinforcement phase in different B<sub>4</sub>C content coatings (vol.%)**

Ceramic phase	B0	B1	B2	B3
TiB <sub>2</sub>	1.5	2.0	8.1	11.9
TiC	10.3	12.5	17.4	20.7
CrB	6.4	17.1	18.3	18.7

2.44, respectively. The standard crystal plane spacing of CrB in the control PDF card was 1.49, 1.26, and 2.35, respectively. It was found that the data gap between the two groups was small. The small increase of crystal plane spacing might be due to lattice distortion caused by the solid solution of a small amount of Ti and Ni elements. Finally, it was determined that the long strip phase rich in Cr and B elements was CrB. A block phase with smooth edges could be observed in Fig. 5a, and the selected area diffraction picture of the block phase is shown in Fig. 5d. The results showed that the spacing of (200) and (220) crystal planes were 2.17 and 1.55, respectively. The standard crystal plane spacing of TiC in the control PDF card was 2.16, and 1.53, respectively, so the crystal plane spacing was slightly increased, which was presumed to be caused by B element in the solid solution part. A bulky phase in the form of regular polygons,

accompanied by dislocations, can be observed in Fig. 5b. Compared with the EDS images under the scanning electron microscope, it was found that it was similar to the block rich in Ti and B elements. Figure 5e shows the diffraction picture of its selected area. The results showed that the spacing of (002), (102), and (100) crystal planes were 1.59, 1.35, and 2.58, respectively. The standard crystal plane spacings of TiB<sub>2</sub> in the control PDF card were 1.61, 1.38, and 2.63, respectively. Combined with EDS elemental analysis, this was determined to be TiB<sub>2</sub>.

### Microhardness Analysis

Figure 6 shows the microhardness distribution of the coating from the substrate to the coating surface with different amounts of B<sub>4</sub>C added (0 wt.%, 3 wt.%, 6 wt.%, 9 wt.%). The large fluctuations of hardness might be due to the difference in hardness between ceramic reinforced phase particles and softer matrix phase. The average microhardness of the cladding layer of the B0 sample without B<sub>4</sub>C addition was 1031.8 HV<sub>0.2</sub>. With the increase of B<sub>4</sub>C addition, the average microhardness of the coating increased to 1087.1, 1203.6, and 1250.3 HV<sub>0.2</sub>, respectively. The average hardness of the B3 sample with the highest average hardness was 15% higher than that of the B0 sample without B<sub>4</sub>C addition. The main reason was that the added B<sub>4</sub>C

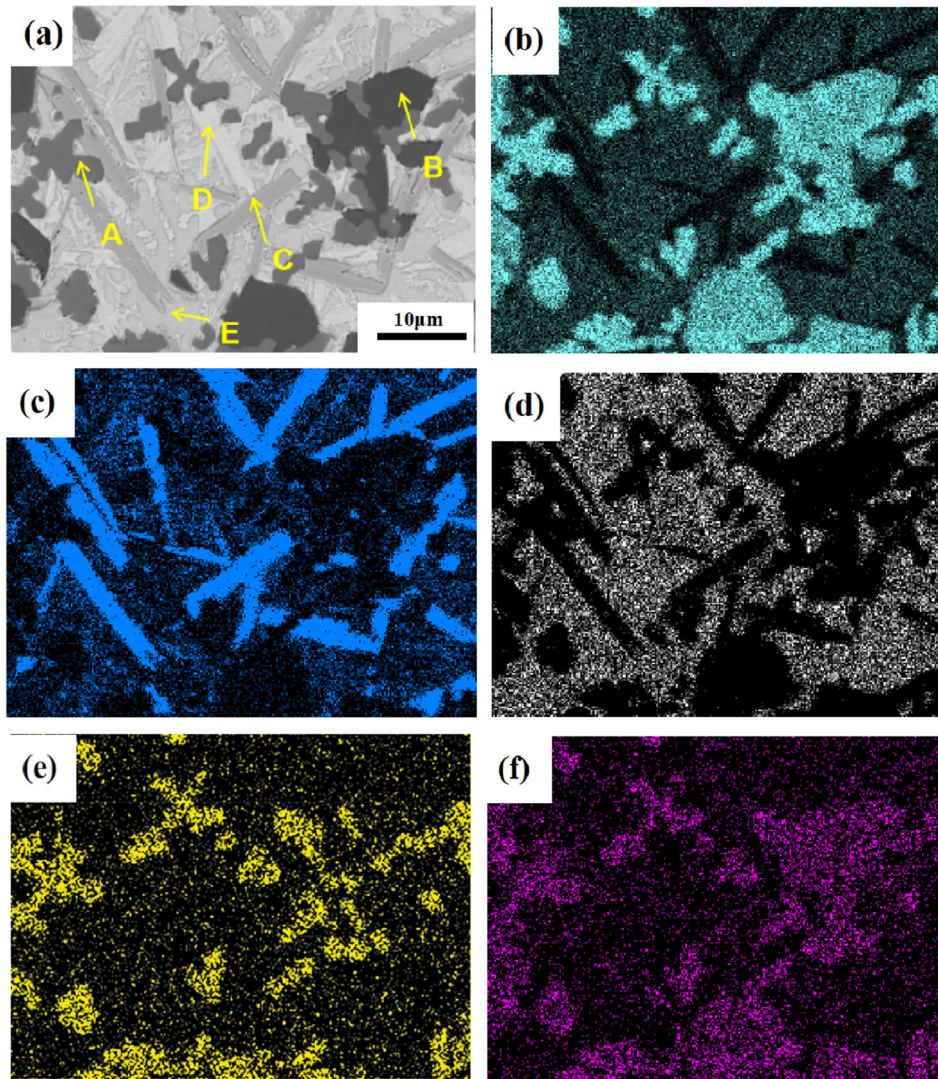


Fig. 4. EDS scanning results of different elements in B2 cladding coating: (a) BSE image; (b) Ti; (c) Cr; (d) Ni; (e) C; (f) B.

Table III. EDS elemental analysis of different positions marked in Fig. 4a (at.%)

Marked locations	Ti	B	C	Cr	Ni	Al	Si	Fe
A	53.60	21.45	24.95	–	–	–	–	–
B	37.04	61.38	–	1.58	–	–	–	–
C	3.05	39.26	1.82	43.15	6.34	1.67	1.09	3.61
D	18.33	–	–	6.01	63.27	3.53	1.64	7.22
E	21.49	–	–	5.13	51.67	11.85	5.68	4.17

was decomposed into B and C atoms in the cladding process. C atoms combined with Ti atoms in the molten pool to synthesize more high-hardness reinforcing phase TiC, in situ. At the same time, Ti, Cr, and B elements in the molten pool reacted to form TiB<sub>2</sub>, CrB and other reinforcing phases. The increase of the number and volume of these hard phases improved the overall hardness of the coating.

### Fracture Toughness

The fracture toughness of the coating was determined by using the Vickers indentation method. The indentation morphologies of different coatings were observed under an optical microscope, and the fracture toughness was measured by measuring the crack length caused by the indentation machine. The average fracture toughness of coating B0 was 0.51 MPa m<sup>1/2</sup>. The average fracture toughness of

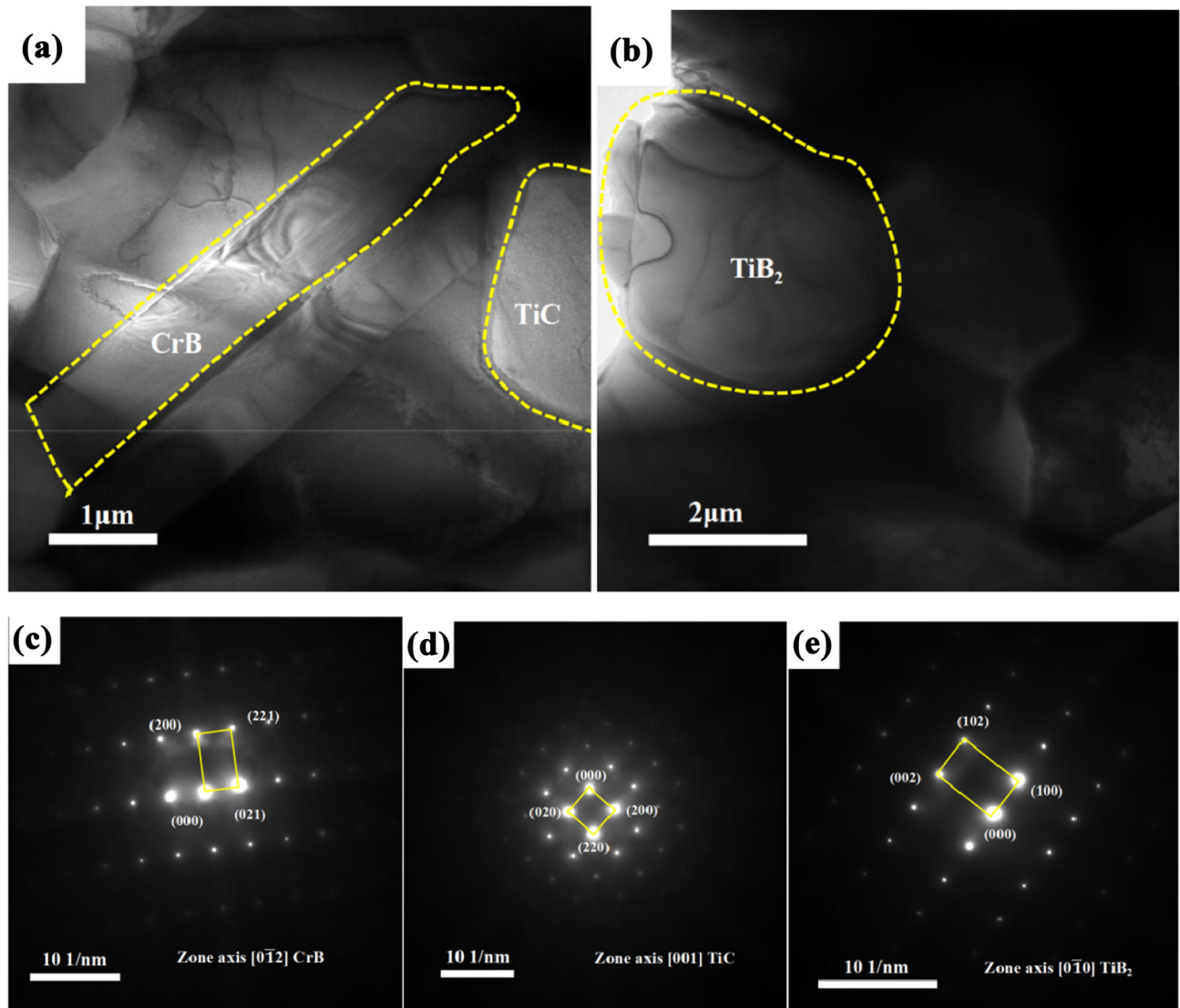


Fig. 5. The TEM of sample B3: (a–b) morphology of CrB, TiC and TiB<sub>2</sub>; (c–e) selected diffraction lattice of CrB, TiC, and TiB<sub>2</sub> ceramic particles.

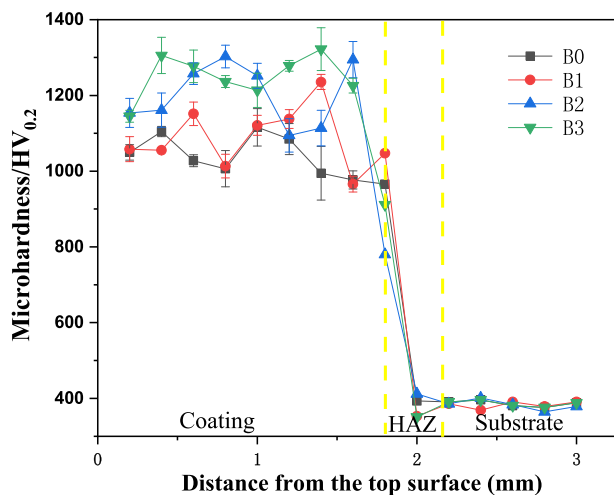


Fig. 6. Microhardness distribution curves of coatings with different B<sub>4</sub>C additions.

coatings B1, B2, and B3 after adding B<sub>4</sub>C were 1.58, 1.42, and 1.24 MPa.m<sup>1/2</sup>, respectively. The above results showed that the fracture toughness of the coating increased and the cracking sensitivity decreased with the addition of B<sub>4</sub>C. However, with the increase of B<sub>4</sub>C content, the fracture toughness decreased gradually. The existence of ceramic materials in metals could hinder crack propagation, thus achieving the effect of strengthening toughness.<sup>27</sup> After the addition of B<sub>4</sub>C, more long CrB and other ceramic phases were formed in the composite coating, which might contribute to crack tip passivation, crack deflection, and bridging.<sup>28</sup> However, the increase in the amount of B<sub>4</sub>C added also increased the size and number of ceramic particles in the coating. The larger the size and number of ceramic particles, the greater the brittleness of the ceramic.<sup>29</sup> In addition, due to the difference of thermal expansion coefficient between ceramic phase and

matrix phase, the increase of reinforcement phase also led to stress concentration and increased the probability of defects in the composite coating. The

increase of reinforcement phase led to the decrease of TiNi with simple cubic structure and  $\gamma$ -Ni phase with good plasticity and toughness in the composite coating, which showed as a decrease of toughness of the composite coating.

### Wear Resistance

Figure 7 shows the wear weight loss of the coating under a 196-N load with different B<sub>4</sub>C addition (0 wt.%, 3 wt.%, 6 wt.%, 9 wt.%). The wear loss of the coating decreased and the wear resistance of the coating increased with the increase of B<sub>4</sub>C addition. When the addition of B<sub>4</sub>C was 9 wt.%, the wear weight loss of the coating was the lowest, which was 1.6 mg, and the wear resistance was the best. The wear resistance of the cladding layer was 33.3% higher than that of the cladding layer without B<sub>4</sub>C addition.

In order to further evaluate and analyze the wear resistance of the coating, the samples were observed

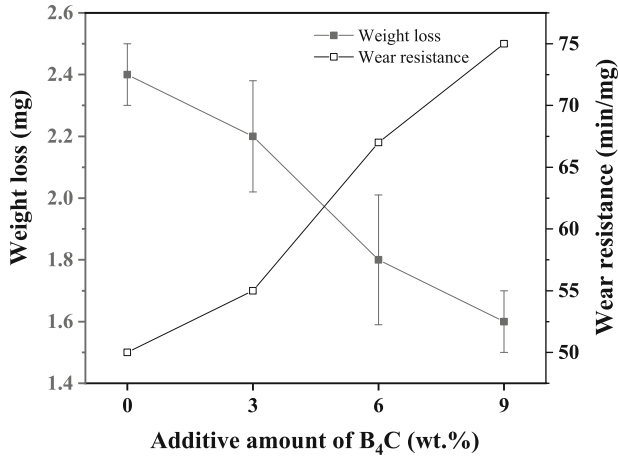


Fig. 7. Effect of B<sub>4</sub>C addition on wear loss and wear resistance of coating.

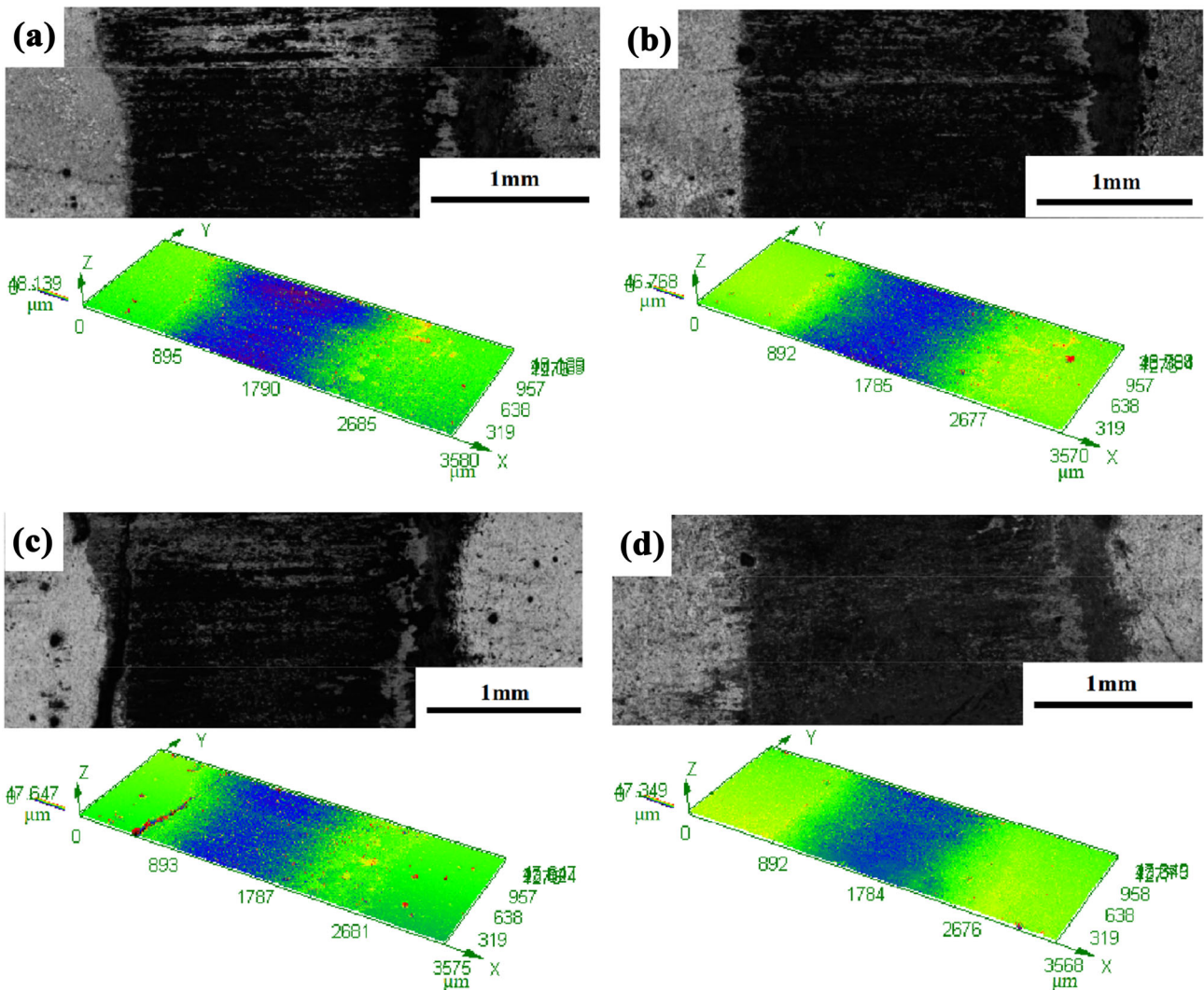


Fig. 8. Worn surface morphology of coating under laser confocal microscope: (a) B0; (b) B1; (c) B2; (d) B3.



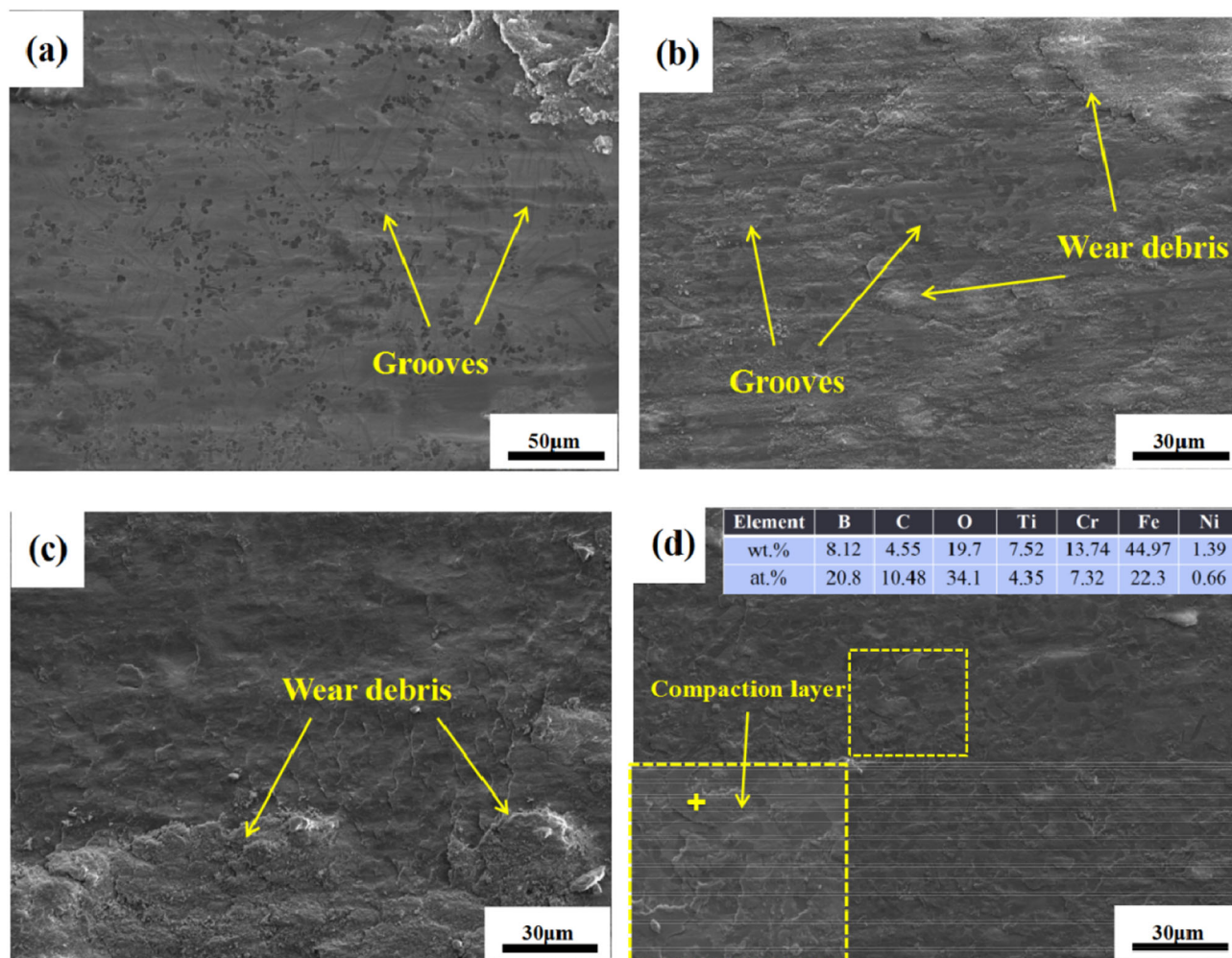


Fig. 9. Wear morphology of coating under 196-N load: (a) B0; (b) B1; (c) B2; (d) B3.

under laser confocal microscope. Figure 8 shows the 3D contour reconstruction of the worn surface. The color contrast in the picture represents the depth difference. It can be seen that, with the addition of B<sub>4</sub>C, the blue parts in the images decreased and the wear depth became shallower. In addition, there were a large number of zigzag peaks and valleys on the worn surface; these furrows showed obvious abrasive wear. With the increase of ceramic reinforcement phase in the coating, in addition to the increase in hardness, the protruding ceramic phase also reduced the contact area between the friction pair and the substrate, and reduced the extent of furrows on the worn surface.

Figure 9 shows the worn surface morphology of the coating under a 196-N load. The main wear failure modes of the cladding layer were adhesive wear and abrasive wear. As shown in Fig. 9a, the coating without B<sub>4</sub>C had furrows and a small amount of debris. The formation of the furrows was mainly due to the existence of hard carbides in the friction ring. Due to the small contact area under the action of pressure, the surface of the

coating was cut during sliding. At the same time, some of the hard particles in the coating continued to cut the friction surface, resulting in a lot of furrows. Indentations due to adhesive wear can also be observed in Fig. 9b. In the process of friction, the surface of the coating was in contact with the grinding ring, and the temperature increased due to the accumulation of friction heat at the interface. Some contact parts might have welded with each other and, as the sliding progressed, the contact points disconnected and were transferred to the surface of the grinding ring. Cracks and lamellar structures caused by surface fatigue due to repeated loading can be clearly seen in Fig. 9c and d, which show the compaction layer produced by repeated compaction of wear debris under the action of friction heat and pressure. The EDS analysis of the dimension points in the diagram showed that there were O and Fe elements in the wear debris. The results showed that the grinding ring material was transferred to the surface of the coating through adhesive wear, accompanied by oxidation wear. The wear debris and compaction layer of the

coating increased after the addition of  $B_4C$ , mainly due to the increase of ceramic reinforcements such as  $TiB_2$ ,  $TiC$ , and  $CrB$  in the coating. After the softer matrix phase in the coating was worn, the ceramic phase was prominent, especially the  $CrB$  ceramic phase with long strips and a large aspect ratio, which was not easy to peel off, and which hindered the formation of furrows. Debris fragments also accumulated in the spaces between hard protruding particles and were compacted in the process of repeated friction to form a compacted layer, as shown in Fig. 9d. It was found that the compacted layer was also concentrated near the ceramic phase. These compacted layers played a protective role and helped to reduce the wear of the coating. Periodically, the ceramic phase broke under the wear load and, at the same time, the compacted layer became worn and the coating was exposed; then the wear process continued. The existence of reinforcing phase in the cladding layer improved the hardness of the cladding layer and increased the compression yield limit, which led to an improvement of adhesive wear resistance of the coating. With the increase of  $B_4C$  addition, the microhardness increased from 1152.9 HV to 1265.1  $HV_{0.2}$ , and the fracture toughness decreased from  $1.58 \text{ MPa m}^{1/2}$  to  $1.24 \text{ MPa m}^{1/2}$ . High hardness improved resistance to micro-cutting. Low fracture toughness increased the occurrence of brittle debonding. Overall, wear resistance was enhanced under these different actions.

## CONCLUSION

- (1) In the laser cladding composite coatings with different  $B_4C$  content, the main phases were  $\gamma$ -Ni,  $Ni_3Ti$ ,  $NiTi$ ,  $TiB_2$ ,  $TiC$ , and  $CrB$ . With the increase of  $B_4C$  addition, the strip-like  $CrB$  phase in the coating increased obviously.
- (2) With the increase of  $B_4C$  addition, the average microhardness of the coating increased gradually. The average hardness of the B3 sample was 15% higher than that of the B0 sample without  $B_4C$  addition.
- (3) The average fracture toughness of the coating B0 was only  $0.51 \text{ MPa m}^{1/2}$ . With the addition of  $B_4C$ , the fracture toughness of the composite coating was significantly improved and increased to  $1.24\text{--}1.58 \text{ MPa m}^{1/2}$ .
- (4) With the increase of  $B_4C$  addition, the wear weight loss of the composite coating decreased and the wear resistance increased. When the addition of  $B_4C$  was 9 wt.%, the wear resistance of the cladding layer was 33.3% higher than that of the cladding layer without  $B_4C$  addition.

## ACKNOWLEDGEMENTS

The authors would like to thank R&D Program of Beijing Municipal Education Commission (KZ202210005004) for financial support for this work.

## CONFLICT OF INTEREST

The authors declare that they have no conflicts of interest.

## REFERENCES

1. R. Sahoo, B.B. Jha, T.K. Sahoo, and D. Sahoo, *J. Mater. Eng. Perform.* 23, 2092. <https://doi.org/10.1007/s11665-014-0987-7> (2014).
2. H. Dong and T. Bell, *Wear* 238, 131. [https://doi.org/10.1016/S0043-1648\(99\)00359-2](https://doi.org/10.1016/S0043-1648(99)00359-2) (2000).
3. R. Srinivasan, M. Kamaraj, D. Rajeev, S. Ravi, and N. Senthilkumar, *Silicon* 14, 8629. <https://doi.org/10.1007/s12633-022-01657-z> (2022).
4. A. Vadiraj and M. Kamaraj, *Mater. Sci. Forum* 681, 539. <https://doi.org/10.4028/www.scientific.net/MSF.539-543.681> (2007).
5. Y. Luo, S. Ge, Z. Jin, and J. Fisher, *P I Mech. Eng. J-J Eng. Tribol.* 223, 311. <https://doi.org/10.1243/13506501JET488> (2009).
6. S. Mukherjee, S. Dhara, and P. Saha, *J. Manuf. Process.* 65, 119. <https://doi.org/10.1016/j.jmapro.2021.03.023> (2021).
7. H.X. Zhang, H.J. Yu, and C.Z. Chen, *Sci. Eng. Compos. Mater.* 24, 541. <https://doi.org/10.1515/secm-2015-0032> (2017).
8. Y. Zhu, X.B. Liu, Y.F. Liu, G. Wang, Y. Wang, Y. Meng, and J. Liang, *Surf. Coat. Technol.* 424, 127664. <https://doi.org/10.1016/j.surfcoat.2021.127664> (2021).
9. Z.Y. Zhou, X.B. Liu, S.G. Zhuang, X.H. Yang, M. Wang, and C.F. Sun, *Appl. Surf. Sci.* 481, 209. <https://doi.org/10.1016/j.apsusc.2019.03.092> (2019).
10. W.L. Li, R.F. Di, R.W. Yuan, H.Y. Song, and J.B. Lei, *J. Manuf. Process.* 74, 413. <https://doi.org/10.1016/j.jmapro.2021.12.045> (2022).
11. Y.L. Xia, H.N. Chen, X.D. Liang, and J.B. Lei, *J. Manuf. Process.* 68, 1694. <https://doi.org/10.1016/j.jmapro.2021.06.074> (2021).
12. N.S. Karthiselva and S.R. Bakshi, *Mater. Sci. Eng. A* 663, 38. <https://doi.org/10.1016/j.msea.2016.03.098> (2016).
13. Y.H. Liu, *Study on Fabrication and Reinforcement Mechanism of Ni-based Composite Laser Cladding Coating on Ti6Al4V Alloy*. East China University of Science and Technology, 2015 (in Chinese).
14. L.L. Bai, J. Li, J.L. Chen, R. Song, J.Z. Shao, and C.C. Qu, *Opt. Laser Technol.* 76, 33. <https://doi.org/10.1016/j.optlastec.2015.07.010> (2016).
15. Y. Diao and K. Zhang, *Appl. Surf. Sci.* 352, 163. <https://doi.org/10.1016/j.apsusc.2015.04.030> (2015).
16. M.G. Krukovich, B.A. Prusakov, and I.G. Sizov, The formation conditions for boride and boronized layers and their influence on the layers' plasticity. in *Plasticity of Boronized Layers*, vol 237 (Cham, Springer Series in Materials Science, 2016) pp. 81–110. [https://doi.org/10.1007/978-3-319-40012-9\\_7](https://doi.org/10.1007/978-3-319-40012-9_7).
17. Q.W. Meng, L. Geng, and B.Y. Zhang, *Surf. Coat. Technol.* 200, 4923. <https://doi.org/10.1016/j.surfcoat.2005.04.059> (2006).
18. X.H. Fan, L. Geng, B. Xu, and J. Li, *Adv. Mater. Res.* 79, 473. <https://doi.org/10.4028/www.scientific.net/AMR.79-82.473> (2009).
19. Y.L. Liang, H.G. Fu, Z.G. Xing, X.Y. Guo, and J. Lin, *J. Mater. Eng. Perform.* 31, 5189. <https://doi.org/10.1007/s11665-022-06604-y> (2022).

20. M. Masanta, S.M. Shariff, and A.R. Choudhury, *Mater. Sci. Eng. A* 528, 5327. <https://doi.org/10.1016/j.msea.2011.03.057> (2011).
21. W.G. Li, J. Li, and Y.S. Xu, *Coatings* 11, 960. <https://doi.org/10.3390/coatings11080960> (2021).
22. C.C. Qu, J. Li, L.L. Bai, J.Z. Shao, R. Song, and J.L. Chen, *J. Alloys Compd.* 644, 450. <https://doi.org/10.1016/j.jallcom.2015.05.081> (2015).
23. J.M. Drezet, S. Pellerin, C. Bezençon, and S. Mokadem, *J. Phys. IV* 120, 299. <https://doi.org/10.1051/jp4:2004120034> (2004).
24. J. Li, X.J. Zhang, H.P. Wang, and M.P. Li, *Int. J. Min. Met. Mater.* 20, 57. <https://doi.org/10.1007/s12613-013-0693-8> (2013).
25. T. Chen, W.P. Li, D.F. Liu, Y. Xiong, and X.C. Zhu, *Ceram. Int.* 47, 755. <https://doi.org/10.1016/j.ceramint.2020.08.186> (2020).
26. E.B. Jacob and P. Garik, *Nature* 343, 523. (1990).
27. A. Faye, V. Paramesw, and S. Basu, *Mech. Mater.* 94, 156. <https://doi.org/10.1016/j.mechmat.2015.12.002> (2016).
28. Q. Chang, D.L. Chen, H.Q. Ru, X.Y. Yue, L. Yu, and C.P. Zhang, *Biomaterials* 31, 1493. <https://doi.org/10.1016/j.biomaterials.2009.11.046> (2010).
29. J.D. Hogan, L. Farbaniec, T. Sano, M. Shaeffer, and K.T. Ramesh, *Acta Mater.* 102, 263. <https://doi.org/10.1016/j.actamat.2015.09.028> (2016).

**Publisher's Note** Springer Nature remains neutral with regard to jurisdictional claims in published maps and institutional affiliations.

Springer Nature or its licensor (e.g. a society or other partner) holds exclusive rights to this article under a publishing agreement with the author(s) or other rightsholder(s); author self-archiving of the accepted manuscript version of this article is solely governed by the terms of such publishing agreement and applicable law.